Strongly and weakly self-similar diffusion

R. Ferrari [a,*], A.J. Manfroi [b], W.R. Young [b]

[a] *Woods Hole Oceanographic Institution, MS#21, Woods Hole, MA 02543, USA*
[b] *Scripps Institution of Oceanography, University of California at San Diego, La Jolla, CA 92093-0213, USA*

Abstract

Many dispersive processes have moments of displacements with large-t behavior $\langle |x|^p \rangle \sim t^{\gamma_p}$. The study of γ_p as a function of p provides a more complete characterization of the process than does the single number γ_2. Also at long times, the core of the concentration relaxes to a self-similar profile, while the large-x tails, consisting of particles which have experienced exceptional displacements, are not self-similar. Depending on the particular process, the effect of the tails can be negligible and then γ_p is a linear function of p (strong self-similarity). But if the tails are important then γ_p is a non-trivial function of p (weak self-similarity). In the weakly self-similar case, the low moments are determined by the self-similar core, while the high moments are determined by the non-self-similar tails. The popular exponent γ_2 may be determined by either the core or the tails. As representatives of a large class of dispersive processes for which γ_p, is a piecewise-linear function of p, we study two systems: a stochastic model, the "generalized telegraph model", and a deterministic area-preserving map, the "kicked Harper map". We also introduce a formula which enables one to obtain the moment $\langle |x|^p \rangle$ from the Laplace–Fourier representation of the concentration. In the case of the generalized telegraph model, this formula provides analytic expressions for γ_p. © 2001 Elsevier Science B.V. All rights reserved.

Keywords: Diffusion; Fractional moments; Similarity solution; Anomalous; Harper map

1. Introduction

There is mounting evidence, both theoretical [1–5] and experimental [6–8], that some dispersive processes in fluid mechanics can be understood as continuous time random walks in which the motion of particles alternates between sticking events, during which the velocity is essentially zero, and flying events, during which the velocity is approximately uniform. These different behaviors are characteristic of flows which consist of an array of long-lived, quasi-stationary vortices threaded by jets. Particles in the vortices are trapped, while those in the jets fly over large distances. Because the flow is unsteady, particles can pass to-and-fro between the vortices and the jets at apparently random instants. These fluid mechanical examples are of general interest because they provide real examples of Lévy walks, anomalous diffusion, and other topics which are attracting interest in statistical physics [9].

* Corresponding author.
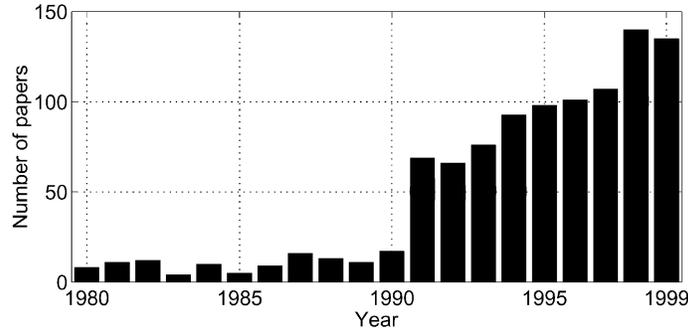*E-mail address:* rferrari@whoi.edu (R. Ferrari).

Fig. 1. Histogram of papers containing the key words "anomalous" and "diffusion" in the title or abstract (Science Citation Index).

1.1. Anomalous diffusion, the central scaling region and the tails

Anomalous diffusion has been the focus of so many studies in the last decade that it is now impossible to provide a comprehensive review of the subject (Fig. 1). Anomalous diffusion is defined in terms of the second moment, or variance, of particle displacements,

$$\langle x^2 \rangle \equiv \frac{1}{N} \sum_{n=1}^{N} x_n^2(t). \tag{1.1}$$

In (1.1), N is the number of tracer particles and $x_n(t)$ is the position of particle n at time t (we assume that $x_n(0) = 0$). In a normal diffusive process $\langle x^2 \rangle \sim t^1$. Anomalous diffusion has $\langle x^2 \rangle \sim t^{\gamma_2}$ with $\gamma_2 \neq 1$. If $\gamma_2 > 1$ the process is superdiffusive while if $\gamma_2 < 1$ the process is subdiffusive.

The dichotomy between normal and anomalous diffusion is based solely on the behavior of the second moment; the majority of the references in Fig. 1 are concerned mostly with that single descriptor of dispersion. However, one often wants to know more than simply $\langle x^2 \rangle(t)$. For example, one would like to possess the Green's function or propagator of the process. It is usually not possible to obtain the propagator exactly, though asymptotic methods often provide useful approximations in the form of similarity solutions. That is to say, as $t \to \infty$, the concentration collapses to the self-similar form,

$$C(x, t) \approx t^{-1/\nu} \mathcal{C}\left(\frac{x}{t^{1/\nu}}\right). \tag{1.2}$$

In the case of normal diffusion $\gamma_2 = 1$, $\nu = 2$ and $\mathcal{C}$ is a Gaussian. In the superdiffusive case there are examples in which $\mathcal{C}$ is a Lévy density (for example [10]). In the subdiffusive case, $\mathcal{C}$ is neither Lévy nor Gaussian (e.g., see [2]).

The approximation in (1.2) is valid only in a *central scaling region* (CSR). The non-scaling tails of the distribution are occupied by particles which have experienced exceptionally large displacements. Sometimes tails are important even though they contain few particles; the sum in (1.1) might be dominated by a few large terms corresponding to tail particles. This problem is strikingly demonstrated when $\mathcal{C}(\xi)$ is a Lévy density which has, for $\xi \gg 1$, a slow algebraic decay: $\mathcal{C}(\xi) \sim \xi^{-\nu-1}$ with $1 < \nu < 2$. Thus, in the Lévy case, the second moment of the similarity approximation (1.2) diverges. But in a simulation or experiment $\langle x^2 \rangle$ is always finite and this problem with the Lévy density is simply the result of incorrectly applying (1.2) outside of the CSR.

To summarize, the tails are not described by (1.2), and there are several important questions suggested by this observation. For instance we have introduced two exponents, γ_2 and $1/\nu$. How are they related? The naive answer

is that $\gamma_2 = 2/\nu$. In fact, $\gamma_2 = 2/\nu$ is correct if $\mathcal{C}$ is a Gaussian, and also in the subdiffusive example in [2]. But $\gamma_2 \neq 2/\nu$ if $\mathcal{C}$ is a Lévy density. How representative of the dispersion of a typical particle are the single statistic $\langle x^2 \rangle$ and the exponent γ_2? Given the results of an experiment or simulation, how can we detect the existence of a CSR and determine the two exponents γ_2 and $1/\nu$? Is the similarity solution in (1.2) the solution of a partial differential equation, or perhaps a "fractional kinetic equation" such as those derived in [2,11]?

1.2. Moments and strong versus weak self-similarity

The general moments, defined by

$$\langle |x|^p \rangle \equiv \frac{1}{N} \sum_{n=1}^{N} |x_n(t)|^p \tag{1.3}$$

provide information about both the CSR and the non-scaling tails. Small values of p sample the CSR, while larger values of p sample the tails. Given the great interest in turbulent structure functions of fractional order (e.g. [12]), it is surprising that $\langle |x|^p \rangle$ has attracted only sporadic attention as a descriptor of diffusion. We located only a few papers which discuss $\langle |x|^p \rangle$ as a continuous function of p in the context of anomalous diffusion [13–17].

Suppose that $\langle |x|^p \rangle$ grows like a power law as $t \to \infty$:

$$\langle |x|^p \rangle \sim t^{\gamma_p}. \tag{1.4}$$

The exponent γ_p, is an important descriptor of the dispersive process, which contains information about both the CSR and the tails of the propagator. In other words, studying the function γ_p, as opposed to the single number γ_2, provides more information, and the possibility of more demanding comparison between theory, simulation and experiment.

Given γ_p we make a distinction between *strong self-similarity* and *weak self-similarity*. We say that a process is strongly self-similar if *all* moments satisfy the scaling law suggested by (1.2). In other words, if $\gamma_p = p/\nu$ for all p then the process is strongly self-similar. If γ_p is a more interesting function of p, such as in Fig. 2, then we say that the process is weakly self-similar. While all diffusive processes have non-scaling tails which defeat (1.2), this defeat is particularly sharp if the process is weakly self-similar.
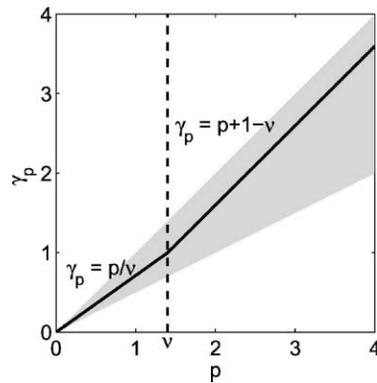

Fig. 2. A schematic illustration of a process which is both weakly self-similar and superdiffusive. The exponent γ_p is a piecewise-linear function of p with a break at $p = \nu$. The shaded wedge is the region between the diffusive law $\gamma_p = \frac{1}{2}p$ and the ballistic law $\gamma_p = p$. Low-order moments, $p < \nu$, are determined by a CSR, in which (1.2) applies. The higher moments, $p > \nu$, are determined by the non-scaling tails of the concentration profile. Since $\nu < 2$ the second moment is determined by the tails of the concentration and determination of γ_2 does not provide information about the dispersion of a typical particle in the CSR.
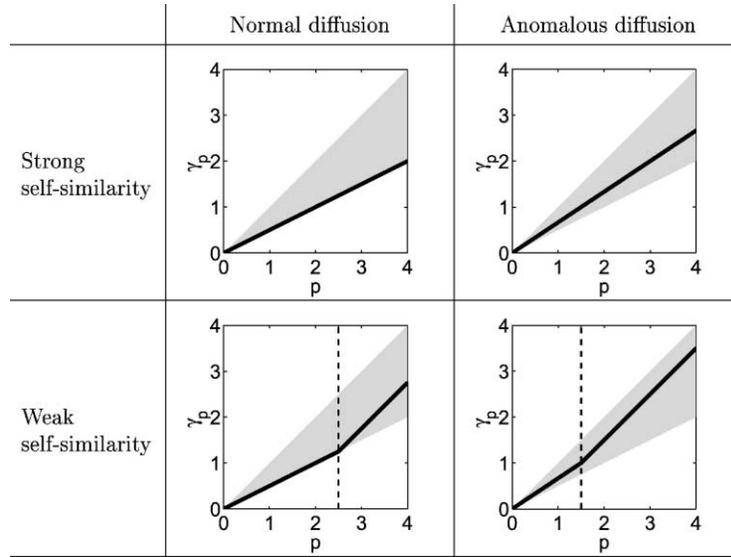
Fig. 3. Classification of processes as normally versus anomalously diffusive, and weakly versus strongly self-similar. In these figures the shaded wedge indicates the region between normal diffusion, $\gamma_p = \frac{1}{2}p$, and ballistic dispersion $\gamma_p = p$. In the bottom row the break in slope is at $p_{\max} = \max[\nu, 2(\nu - 1)]$. The most elementary case is the top left panel, which is exemplified by the telegraph process. The most complicated case is the bottom right panel, which is shown in greater detail in Fig. 2.

The dichotomy between strong and weak self-similarity is independent of the dichotomy between normal and anomalous diffusion. Thus, as indicated in Fig. 3, there are four cases which might occur. In this article we present several models which, depending on parameter settings, fall into each of the four boxes in Fig. 3.

Dynamical systems that display each of the four cases in Fig. 3 can be found in the literature. Pikovsky [14] shows that diffusion in a one-dimensional Lorenz-type map is weakly self-similar, but either normal or anomalous for different choices of the control parameter. Castiglione et al. [16] give examples of both strongly self-similar normal diffusion and weakly self-similar anomalous diffusion in the standard map. Carreras et al. [15] construct a running sandpile model which displays weakly self-similar anomalous diffusion.

Castiglione et al. [16] use the term "strong anomalous diffusion" for the bottom row in Fig. 3. We argue that this term is confusing because in the bottom left panel of Fig. 3, $\langle x^2 \rangle$ exhibits normal diffusive growth. That is, there are processes which are both normally diffusive and weakly self-similar.

1.3. Piecewise-linear γ_p

In Fig. 2, γ_p is a piecewise-linear function of p and the break in slope occurs at $p = \nu$ where $1/\nu$ is the exponent in (1.2). The break in slope at $p = \nu$ is produced by an exchange of dominance between the majority of particles in the CSR, which determine the moments with $p < \nu$, and the exceptional particles in the tails which determine the moments with $p > \nu$. The tail particles have experienced *almost* ballistic motion which is why the line $\gamma_p = p + \nu - 1$ is parallel, but below, the pure ballistic $\gamma_p = p$. This almost ballistic behavior of the high moments is also characteristic of the diffusive case in the bottom left panel of Fig. 3.

Below we give examples, both analytic and numerical, and both deterministic and stochastic, for which γ_p, is a piecewise-linear function of p. We are not claiming that all weakly self-similar processes have the piecewise-linear relation in Fig. 2. For example, Andersen et al. [17] show how to construct stochastic models with a non-piecewise-

linear relation for the moments. But piecewise-linear γ_p is probably the simplest form of weak self-similarity: the break in slope is a clean signature of the exchange of dominance between the CSR and the tails.

1.4. A review of the telegraph model

In this section we review a venerable model of correlated random walks, namely the telegraph model (see [18]). The telegraph model is the basis of the stochastic model in the next section and it also serves as an example of the elementary case in the upper left panel of Fig. 3. The model is particularly instructive because one can obtain a Green's function exactly and exhibit both the CSR and the non-scaling tails explicitly.

In a telegraph process the velocity of a particle has only one of two possible values, $+U$ and $-U$. The velocity flips randomly back and forth between $\pm U$ with a transition probability $\frac{1}{2}\alpha$ per time. Let $R(x, t)$ denote the density (particles/length) of particles moving to the right (with velocity $+U$) and $L(x, t)$ denote the density of particles moving to the left (with velocity $-U$). The coupled conservations laws are

$$R_t + UR_x = \tfrac{1}{2}\alpha(L - R), \qquad L_t - UL_x = \tfrac{1}{2}\alpha(R - L). \tag{1.5}$$

The total concentration is $C \equiv R + L$ and after some simple manipulations one finds from (1.5) that

$$C_{tt} + \alpha C_t - U^2 C_{xx} = 0. \tag{1.6}$$

On large, slowly evolving length-scales one can neglect the term C_{tt} in (1.6) and obtain the diffusion equation, with the diffusivity U^2/α, as an approximation of (1.6).

Using the method of Morse and Feshbach [18], the solution of (1.6) with the initial conditions $C(0, x) = \delta(x)$ and $C_t(0, x) = 0$ is

$$C(x, t) = \frac{1}{2U}\left(\frac{\partial}{\partial t} + \alpha\right) e^{-\alpha t/2} I_0\left[\frac{\alpha}{2U}(U^2 t^2 - x^2)^{1/2}\right] H(Ut - |x|), \tag{1.7}$$

where I_0 is a modified Bessel function and H the Heaviside step function.

The Gaussian similarity approximation, which applies in the CSR, is obtained by taking the double limit $t \to \infty$ with $|x|\alpha^{1/4}/Ut^{3/4} \to 0$ in (1.7). Thus, the tails of $C(x, t)$ span the region

$$\left(\frac{U}{\alpha}\right)(\alpha t)^{3/4} < |x| < Ut. \tag{1.8}$$

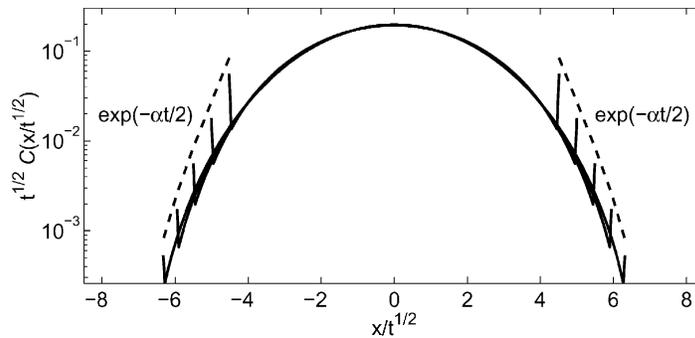Fig. 4. The Green's function in (1.7) at five evenly spaced times with $10 < \alpha t < 20$. In this semi-log plot the Gaussian similarity approximation is a parabola and as t increases the curves collapse onto this parabola. The strongest symptom of the tails are δ-function peaks at $x = \pm Ut$. These ballistic peaks are produced by particles which have traveled with constant velocity since $t = 0$. But the number of these particles decays like $\exp(-\frac{1}{2}\alpha t)$, as indicated by the dashed lines.

The Green's function in (1.7) is plotted using the similarity variable $x/\sqrt{t}$ in Fig. 4. The non-scaling tails fall below the Gaussian approximation except for δ-function peaks at $x = \pm Ut$. These ballistic peaks consist of particles which have traveled with constant velocity since $t = 0$. However, the complete tail-structure of C is more complicated than simply a pair of ballistic peaks at $x = \pm Ut$ the Gaussian similarity approximation fails, and the tails begin, at $x \sim t^{3/4} \ll t$. But, despite the asymptotically expanding zone in (1.8), the moments have $\langle |x|^p \rangle \sim t^{p/2}$ for all p. Thus, this elementary telegraph model is both normally diffusive and strongly self-similar. The tail structure is not self-similar, but the failure of similarity is so mild that as $t \to \infty$ all moments are determined by the CSR.

2. The generalized telegraph model

In this section we develop a generalization of the telegraph model which can be used to illustrate all four cases in Fig. 3. Consider an ensemble of particles, each of which switches randomly between moving with $u(t) = +U$, $u(t) = 0$ and $u(t) = -U$. The transition probabilities between these three states are functions of the time since the last transition. In other words, each particle carries an "age", a, which is the time elapsed since the particle transitioned into its present state. We denote the density of right-moving particles at (x, t), with age a, by $\mathcal{R}(a, x, t)$. For left-moving particles the density is $\mathcal{L}(a, x, t)$, and for the stationary particles the density is $\mathcal{S}(a, x, t)$. Following Solomon et al. [7] we refer to the left- and right-movers collectively as "flying" particles, while the stationary particles are "sticking" particles.

2.1. The conservation laws

The flying particles satisfy the conservation laws

$$\mathcal{R}_t + \mathcal{R}_a + U\mathcal{R}_x + \alpha_{\mathrm{F}}\mathcal{R} = 0, \qquad \mathcal{L}_t + \mathcal{L}_a - U\mathcal{L}_x + \alpha_{\mathrm{F}}\mathcal{L} = 0, \tag{2.1}$$

while the sticking particles have

$$\mathcal{S}_t + \mathcal{S}_a + \alpha_{\mathrm{S}}\mathcal{S} = 0. \tag{2.2}$$

The death rates of flying and sticking particles, α_{F} and α_{S}, respectively, are functions of age a; it is through this device that particles have a memory of their previous history. The price paid for this non-Markovian memory is that there are now three independent variables, (a, x, t). The aging of particles is represented by the advective-terms $\mathcal{R}_a$, $\mathcal{L}_a$, and $\mathcal{S}_a$, which ensure that the density functions move along the a-axis with constant speed, namely one second per second.

Stationary particles are born with $a = 0$ when left- and right-moving particles die. And, conversely, when a stationary particle dies it is reborn as either a left-moving particle or a right-moving particle with equal probability. Notice that in order for a right-moving particle to become a left-moving particle it must pass through the intermediate state with $u = 0$. These karmic rules are enforced by boundary conditions at $a = 0$:

$$\mathcal{L}(0, x, t) = \mathcal{R}(0, x, t) = \frac{1}{2}\int_0^\infty \alpha_{\mathrm{S}}(a)\mathcal{S}(a, x, t)\, \mathrm{d}a, \tag{2.3}$$

and

$$\mathcal{S}(0, x, t) = \int_0^\infty \alpha_{\mathrm{F}}(a)[\mathcal{L}(a, x, t) + \mathcal{R}(a, x, t)]\, \mathrm{d}a. \tag{2.4}$$

The total concentration $C(x, t)$ is the sum over all stationary and flying particles integrated over all ages,

$$C(x, t) \equiv \int_0^\infty [\mathcal{R}(a, x, t) + \mathcal{L}(a, x, t) + \mathcal{S}(a, x, t)] \, da. \tag{2.5}$$

Conservation of particles, enforced through the karmic rules, guarantees that the integral of C in x is constant in time. Here this integral is set to 1 as a normalization condition,

$$\int_{-\infty}^\infty C(x, t) \, dx = 1. \tag{2.6}$$

The system in (2.1) through (2.4) is a generalization of the telegraph model (1.5) in two ways. First, there are three states: left, right and stationary. This embellishment is motivated by experiments [7] in which trapping in a vortex corresponds to the stationary particles, while jets carry particles to both the left and the right. The non-trivial generalization is the introduction of the additional independent variable a which captures memory effects.

Memory effects are implicit in two earlier statistical descriptions of anomalous diffusion. These models, which are fully equivalent to (2.1) through (2.4), are the renewal-process formulation, reviewed by Geisel in [9], and the continuous time random-walk formulation, reviewed by Klafter, Zumofen and Schlesinger, also in [9]. Our preference for the generalized telegraph model is partly a matter of taste and background, because of its similarity to the conservation laws of fluid mechanics, the generalized telegraph model is easy for us to understand. Another point is that there has been some discussion in the literature about how anomalous diffusion might be described by partial differential equations, as opposed to integral equations with memory kernels. The generalized telegraph model is a natural way of achieving a differential equation description, but only by carrying the extra independent variable a.

If α_S and α_F are constants (independent of a) one can simplify (2.1) through (2.2) by integrating over a and using the $a = 0$ boundary conditions in (2.3) and (2.4). One then finds a three-state version of (1.5). To recover precisely (1.5) one can take the limit $\alpha_S \to \infty$ so that the stationary sojourns are very brief. Thus the classical telegraph model is a special case of (2.1) through (2.4).

2.2. The equilibrium solution, and the PDF of flying and sticking durations

To relate the generalized telegraph model to the other statistical descriptions of anomalous diffusion we begin by considering the simplest solution of (2.1) through (2.4). Suppose that the ensemble of N particles has spatially uniform density ($\partial_x = 0$) and that the ensemble is steady ($\partial_t = 0$). This *equilibrium* solution is

$$\mathcal{R}(a, x, t) = \mathcal{L}(a, x, t) = r \Psi_F(a), \qquad \mathcal{S}(a, x, t) = 2r \Psi_S(a), \tag{2.7}$$

where $\Psi_\chi(a)$ is

$$\Psi_\chi(a) \equiv \exp\left(-\int_0^a \alpha_\chi(a') \, da'\right). \tag{2.8}$$

(From now on the subscript χ indicates either F or S.) The constant r in (2.7) is the transition rate between the different states and using the normalization condition in (2.6) we find

$$r = \frac{1}{2(\tau_S + \tau_F)}, \tag{2.9}$$

where

$$\tau_\chi \equiv \int_0^\infty \Psi_\chi(a) \, da. \tag{2.10}$$

The functions Ψ_F and Ψ_S introduced in (2.8) have an important intuitive interpretation:

$$\Psi_F(a) = \text{probability that a flight lasts longer than } a. \tag{2.11}$$

$\Psi_S(a)$ is interpreted analogously. To understand (2.11), notice that in the equilibrium solution (2.7), $\Psi_F(a)$ is the factor by which a cohort of new flyers, with $a = 0$, is reduced by the passage of time till they reach age a. Solomon et al. [7], characterize the duration of flying and sticking events using a probability density function (PDF):

$$\mathcal{P}_F(a)\, da = \text{Probability that a flight has a duration} \in (a, a, +da). \tag{2.12}$$

$\mathcal{P}_S(a)$ is defined analogously. The cumulative distributions, Ψ_χ, are related to the PDFs, $\mathcal{P}_\chi$, by

$$\mathcal{P}_\chi = -\frac{d\Psi_\chi}{da} = a_\chi \Psi_x. \tag{2.13}$$

The result above is crucial because, given observations of $\mathcal{P}_\chi$, Eq. (2.13) can be used to determine the transition rates α_χ in the generalized telegraph model. We also use (2.13) to interpret τ_χ in (2.10) as the duration of the average sojourn in the flying and sticking states. That is, after integration by parts, it follows from the definition in (2.10) that

$$\tau_\chi = \int_0^\infty a \mathcal{P}_\chi(a)\, da. \tag{2.14}$$

Note that the integral in (2.14) may or may not converge depending on the form of $\alpha_\chi(a)$ at large values of a. If the integral does not converge, then the equilibrium distribution in (2.8) is not normalizable.

2.3. A model for the transition rate, $\alpha_\chi(a)$

To complete the formulation of the generalized telegraph model we must specify the dependence of the transition rates α_F and α_S on a. Our guide here is the experiments of Solomon et al. [7], which show that as $a \to \infty$, the PDFs $\mathcal{P}_F(a)$ and $\mathcal{P}_S(a)$ defined in (2.12) have algebraically decaying tails:

$$\mathcal{P}_\chi(a) \sim a^{-\mu_\chi}, \tag{2.15}$$

with $2 < \mu_\chi < 3$. With these values of μ_χ the integral defining τ_χ in (2.14) converges while the variance, $\int a^2 \mathcal{P}_\chi(a)\, da$, diverges.

Examination of the large-a behavior of (2.13) shows that in order for the generalized telegraph model to reproduce (2.15) the transition rates α_χ must decay like $(\mu_\chi - 1)/a$ when a is large. Thus, we adopt the simple form,

$$\alpha_\chi(a) = \frac{\nu_\chi}{\theta_\chi + a}, \tag{2.16}$$

where $\nu_\chi = \mu_\chi - 1$. The model in (2.16) lends itself to simple illustrative calculations with asymptotic (as $t \to \infty$) limits which are representative of all transition rates with the large-a decay $\alpha_\chi \sim \nu_\chi/a$.

To summarize: Eq. (2.16) adjusts the large-a behavior of α_χ so that the power-law decay of $\mathcal{P}_F$ and $\mathcal{P}_S$ matches experimental results. One can make a dimensional argument in support of (2.16): α_F and α_S have the dimensions of inverse time. If the only time-scale relevant for long-lived particles is the particle age, a, then it follows that α_F and α_S are inversely proportional to a.

With the choice in (2.16) the cumulative distributions, Ψ_χ are given by

$$\Psi_\chi = \left(\frac{\theta_\chi}{\theta_\chi + a}\right)^{\nu_\chi}, \tag{2.17}$$

and the integral in (2.14) converges to $\tau_\chi = \theta_\chi/(\nu_\chi - 1)$ provided that $\nu_\chi > 1$.

2.4. The Laplace–Fourier solution of the initial value problem

Now that we have completed the formulation of the generalized telegraph model we turn to the initial value problem posed by (2.1) through (2.4) with the age-dependent transition rates $\alpha_\chi(a)$ in (2.16). As an initial condition we assume that $\tau_\chi < \infty$ and we use

$$[\mathcal{R}(a, x, 0), \mathcal{S}(a, x, 0), \mathcal{L}(a, x, 0)] = r[\Psi_F(a), 2\Psi_S(a), \Psi_F(a)]\delta(x). \tag{2.18}$$

Thus, all of the particles are released at $x = 0$ with the equilibrium age distribution in (2.7).

The choice of the initial age distribution is one of the more annoying technical details in the formulation of the stochastic model. One expects that the gross details of the dispersion process, such as the scaling exponent γ_p, are independent of the initial distribution of ages. To a large extent this is the case. For example, one can take $\mathcal{R} \propto \delta(a)$, etc. as the initial condition, and obtain the same large-t results as with (2.18). However if one takes an initial age distributions in which there is a very large proportion of very old particles (e.g., power laws which decay more slowly than $\Psi_\chi(a)$) then the large-t results can differ qualitatively from those obtained with (2.18). We mention this uncomfortable possibility because there are cases, such as the deterministic map in Section 5, in which one does not have control over the initial age distribution.

The initial value problem posed with (2.18) can be solved by Fourier transforming in space and Laplace transforming in time. We start by introducing some notation. The Laplace–Fourier transform of any function of x and t, e.g. $C(x, t)$ in (2.5), is defined as

$$C(k, \eta) \equiv \int_0^\infty dt \int_{-\infty}^\infty dx \, e^{-\eta t - ikx} C(x, t). \tag{2.19}$$

We use the convention that the arguments indicate the space in which the functions are defined, e.g. $C(k, \eta)$ is the Laplace–Fourier transform of $C(x, t)$. The Laplace transform of any function of age, such as the equilibrium age distributions $\Psi_\chi(a)$, is defined as

$$\Psi_\chi(\eta) \equiv \int_0^\infty e^{-\eta a} \Psi_\chi(a) \, da. \tag{2.20}$$

For convenience we define the combinations $\Psi_F^\pm(\eta, k) \equiv \Psi_F(\eta \pm ikU)$ and

$$\Sigma(k, \eta) \equiv \tfrac{1}{2}[\Psi_F^+ + \Psi_F^-], \qquad \Delta(k, \eta) \equiv \frac{1}{2}\frac{ikU}{\eta}[\Psi_F^+ - \Psi_F^-]. \tag{2.21}$$

The total concentration of particles $C(k, \eta)$ is then

$$C(k, \eta) = C_1(k, \eta) + C_2(k, \eta), \tag{2.22}$$

where

$$C_1(k, \eta) = r \left[\frac{\tau_F - \Psi_F^+}{\eta + ikU} + 2\frac{\tau_S - \Psi_S(\eta)}{\eta} + \frac{\tau_F - \Psi_F^-}{\eta - ikU} \right], \tag{2.23}$$

and

$$C_2(k, \eta) = \frac{2r}{\eta} \frac{(\Sigma + \Psi_S)(\Sigma + \Psi_S - \eta\Psi_S\Sigma) - \eta\Psi_S^2\Delta}{\Sigma + \Psi_S + \Delta - \eta\Psi_S(\Sigma + \Delta)}. \tag{2.24}$$

In (2.23) and (2.24) all variables are in the transform space, e.g., $\Psi_S = \Psi_S(\eta)$. A sketch of the steps that lead to the Laplace–Fourier solution of the initial value problem is given in Appendix A.

The transform $C_1(k, \eta)$ can be inverted to yield

$$C_1(x, t) = r\delta(x - Ut)\Phi_F + 2r\delta(x)\Phi_S + r\delta(x + Ut)\Phi_F, \tag{2.25}$$

where

$$\Phi_\chi(t) \equiv \int_t^\infty \Psi_\chi(t')\,dt'. \tag{2.26}$$

At large times $\Phi_\chi \sim t^{1-\nu_\chi}$ and consequently the δ-function peaks in $C_1(x, t)$ decay algebraically in time. These slowly decaying peaks consist of particles that have never transitioned from their original state. That is to say, the δ-function peak at $x = Ut$ in (2.25) consists of particles which started at $t = 0$ with $u = +U$ and never stopped. The elementary telegraph model from the introduction also displays such ballistic peaks, but in that case the δ-function peaks decay exponentially in time (Fig. 4).

2.5. The second moment: normal versus anomalous diffusion

From (2.22) through (2.24) we obtain an exact result for $\langle x^2 \rangle$. The second moment in transform space is given by

$$\langle x^2 \rangle(\eta) = -\left.\frac{d^2}{dk^2}C(k, \eta)\right|_{k=0} = 4U^2 r\frac{\tau_F - \Psi_F(\eta)}{\eta^3}. \tag{2.27}$$

Inverting the Laplace transform in (2.27) we obtain

$$\langle x^2 \rangle(t) = 4U^2 r \int_0^t (t - a)\Phi_F(a)\,da, \tag{2.28}$$

where $\Phi_F(t)$ is defined in (2.26). If the right-hand side of (2.28) grows linearly in time as $t \to \infty$ then the variance grows diffusively. Otherwise there is anomalous diffusion.

With (2.28) in hand, one can easily determine if particular models of α_F and Ψ_F lead to anomalous diffusion. For example, using $\alpha_F(a)$ in (2.16), and evaluating the integral in (2.28), gives an exact solution

$$\langle x^2 \rangle = \frac{4U^2 r\theta_F^3}{(\nu_F - 1)(2 - \nu_F)}\left[\frac{(1 + \tilde{t})^{3-\nu_F}}{3 - \nu_F} - \tilde{t} - \frac{1}{3 - \nu_F}\right], \tag{2.29}$$

where $\tilde{t} \equiv t/\theta_F$. The transition between anomalous and normal diffusion is obtained as a simple exchange of dominance between the two power laws on the right-hand side of (2.29). Also, despite appearances, (2.29) is valid at $\nu_F = 2$ and $\nu_F = 3$ when logarithmic terms, such as $t \ln t$, appear if one takes the limit. Notice the minor role of $\alpha_S(a)$ in (2.29) provided that $\nu_S > 1$, so that τ_S is finite, then the parameters ν_S and θ_S occur only in r. Finally, if $1 < \nu_F < 2$ then (2.29) shows that $\langle x^2 \rangle \propto t^{3-\nu_F}$ and there is superdiffusion.

2.6. Fractional moments: strong versus weak self-similarity

Moments of fractional order can be computed from the expressions for the concentration in (2.22) through (2.24). The contribution to $\langle |x|^p \rangle$ from ballistic particles in $C_1(x, t)$ is

$$\langle |x|^p \rangle_1 = 2rU^p t^p \Phi_F(t). \tag{2.30}$$

Since the moment $\langle |x|^p \rangle$ contains also the positive contribution from C_2, $\langle |x|^p \rangle_1$ is a lower bound on the growth rate of fractional moments. Thus, using the particular model of $\alpha_\chi(a)$ in (2.16), we have

$$\langle |x|^p \rangle > \langle |x|^p \rangle_1 = \frac{2rU^p\theta_F^{\nu_F}}{\nu_F - 1}\frac{t^p}{(\theta_F + t)^{\nu_F - 1}}. \tag{2.31}$$

For large times the right-hand side of (2.31) is proportional to $t^{p+1-\nu_F}$. Though (2.31) is only an inequality, we show below that moments with $p > \nu_F$ do, in fact, have the exponent $p + 1 - \nu_F$.

We can obtain an expression for the Laplace transform of $\langle |x|^p \rangle$ by noticing that

$$|x|^p = \frac{2}{\pi} \Gamma(p+1) \sin \frac{\pi p}{2} \int_0^\infty \frac{1 - \cos x\zeta}{\zeta^{p+1}} \, \mathrm{d}\zeta \quad \text{for } 0 < p < 2. \tag{2.32}$$

Combining (2.32) with the Laplace–Fourier representation of $C(x, t)$, and taking advantage of the symmetry $C(k, \eta) = C(-k, \eta)$, we find, for $0 < p < 2$,

$$\langle |x|^p \rangle(\eta) = \frac{2}{\pi} \Gamma(p+1) \sin \frac{\pi p}{2} \int_0^\infty [C(0, \eta) - C(k, \eta)] \frac{\mathrm{d}k}{k^{p+1}}. \tag{2.33}$$

With (2.33) in hand we can study the asymptotic behavior of the fractional moments without having to invert $C(k, \eta)$. This is an important simplification because the integral in (2.33) eliminates singularities in the complex-η plane, so that the asymptotics of the Laplace transform is more transparent.

As a simple example of singularity elimination, consider the Laplace–Fourier transform $C(k, \eta) = 1/\sqrt{k^2 + \eta^2}$. A direct assault on the inverse Laplace transform using a Bromwich contour requires evaluation of the branch-point singularities at $\eta = \pm ik$. And then one must still invert the Fourier transform. However, using (2.33), we have

$$\langle |x|^p \rangle(\eta) = \frac{2}{\pi} \Gamma(p+1) \sin \frac{\pi p}{2} \eta^{-p-1} \int_0^\infty \left[1 - \frac{1}{\sqrt{1 + \xi^2}} \right] \frac{\mathrm{d}\xi}{\xi^{p+1}}. \tag{2.34}$$

Thus we can invert the Laplace transform without evaluating the integral and conclude that $\langle |x|^p \rangle \propto t^p$.

With the complicated Laplace–Fourier transform in (2.22) through (2.24) it is not possible to slide all η's outside the integral, as we did in (2.34). Nonetheless, since we are concerned only with the large t, or small η, behavior of $\langle |x|^p \rangle$ we can use asymptotic methods to approximate the right-hand side of (2.33). In this way we find that

$$\langle |x|^p \rangle(\eta) \sim D_1 \eta^{-\beta_1} + D_2 \eta^{-\beta_2} + \cdots \tag{2.35}$$

with $\beta_1(p, \nu_\chi) > \beta_2(p, \nu_\chi) > \cdots$. Then, appealing to Watson's lemma for loop integrals, we have

$$\langle |x|^p \rangle \sim D_1 \frac{t^{\beta_1 - 1}}{\Gamma(\beta_1)} + D_2 \frac{t^{\beta_1 - 1}}{\Gamma(\beta_2)} + \cdots \tag{2.36}$$

as $t \to \infty$. The largest exponent is $\gamma_p = \beta_1 - 1$. The heavy algebraic details, which devolve to determining the expansion in (2.35), are given in Section 3 for the case $1 < \nu_\chi < 2$. The same method can be used to determine γ_p for the case $2 < \nu_F$ and $1 < \nu_S$, by extending the formula in (2.33) for $2 < p < 4$.

The main result of the analysis outlined above is the following expression for γ_p:

$$\gamma_p = \begin{cases} \dfrac{p}{\nu_{\min}} & \text{if } p < p_{\max}, \\ p + 1 - \nu_F & \text{if } p > p_{\max}, \end{cases} \tag{2.37}$$

where

$$\nu_{\min} = \min(2, \nu_F), \tag{2.38}$$

and

$$p_{\max}(\nu_F) = \max[\nu_F, 2(\nu_F - 1)]. \tag{2.39}$$

The results above assume that both ν_F and ν_S are greater than 1 so that τ_χ in (2.14) is finite. Surprisingly enough, the statistics of the sticking particles do not appear in the piecewise-linear scaling of the moment exponents. In Sections (3.4) and (3.5) we give analytic expressions for γ_p, for the cases when either ν_F or ν_S are less than 1.

The piecewise-linear scaling in (2.37) through (2.39) is the simplest example of weak self-similarity. Strong self-similarity is found if $\nu_F \to 1$: dispersion becomes ballistic and $\gamma_p = p$ for all p. If $\nu_F \to \infty$, with $\tau_F = \theta_F/(\nu_F - 1)$ fixed, then α_F is independent of age. In this case diffusion is normal and $\gamma_p = \frac{1}{2}p$ for all p. These two strongly self-similar limits correspond to the straight lines which bound the shaded wedge in Fig. 2.

3. Asymptotics

3.1. The small (k, η)-approximation with $1 < \nu_F < 2$ and $1 < \nu_S < 2$

Asymptotic methods are necessary in order to extract information from the expressions for the concentration in (2.22) through (2.24). In this section we limit the analysis to the case $1 < \nu_F < 2$ and $1 < \nu_S < 2$.

The general view is that the concentration $C(x, t)$ collapses towards a self-similar scaling at large scales and long times (e.g. [2,10,11,19]). Therefore the CSR may be obtained as a small (k, η)-approximation of $C(k, \eta)$. The small (k, η)-limit of (2.23) plus (2.24) is

$$C(k, \eta) \approx \frac{1 - q_F[2\Lambda_{\nu_F-1} - \eta\Lambda_{\nu_F-2}] - 2q_S\eta^{\nu_S-1}}{\eta - q_F\Lambda_{\nu_F} - 2q_S\eta^{\nu_S}}, \tag{3.1}$$

where

$$\Lambda_\beta(\eta, k) \equiv (\eta + ikU)^\beta + (\eta - ikU)^\beta, \tag{3.2}$$

and

$$q_\chi \equiv r\tau_\chi\theta_\chi^{\nu_\chi-1}\Gamma(2 - \nu_x). \tag{3.3}$$

In (3.1) η and k are both small, but no assumption has been made about their relative order. Notice that we neglected terms proportional to η in the numerator and to η^2 and $(kU)^2$ in the denominator. These terms are important at leading order for $2 < \nu_F$, but not for $1 < \nu_F < 2$.

At $k = 0$ the expression in (3.1) reduces to $1/\eta$, corresponding to particle number conservation. The structure of (3.1) follows from $\alpha_F \sim \nu_F/a$ and does not depend on the small-a behavior of α_F; that is the long-time and large-scale distribution of particles depends only on the large-a structure α_F.

In Fig. 5 we compare the small (k, η)-approximation in (3.1) with the full analytical solution obtained by computing numerically the Laplace transform of (2.17) and plugging it into (2.22) through (2.24). The Laplace–Fourier solutions are plotted as a function of kU for $\eta = 10^{-4}$. The two curves are extremely close for small Uk, but diverge for $Uk > 10^{-2}$ (see Fig. 5a). As it turns out, the large-k structure of $C(k, \eta)$ does not play a role in the scaling of fractional moments at leading order, and the approximation in (3.1) contains all the necessary information to compute γ_p.

3.2. The Lévy core of the propagator for $1 < \nu_F < 2$ and $1 < \nu_S < 2$

The propagator in (3.1) cannot be inverted analytically. A more tractable expression is obtained by considering only wavenumbers $|kU| \gg \eta$, so that $(\eta \pm ikU)^\beta \approx (\pm ikU)^\beta$. In other words we take the limit of $C(k, \eta)$ in (2.22)
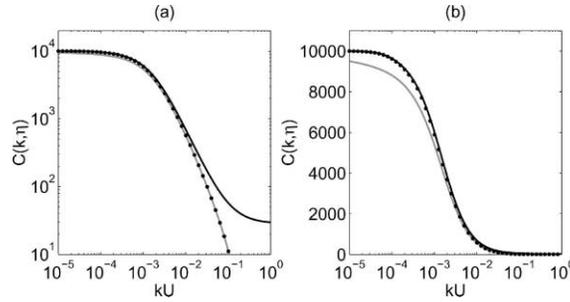
Fig. 5. The concentration $C(k, \eta)$ in Laplace–Fourier space for $\eta = 10^{-4}$. (a) The continuous black curve is the full solution. The dotted curve is the small (k, η)-approximation in (3.1) and the continuous gray curve is the simpler approximation in (3.4). (b) Same as in (a) but on a linear versus logarithmic scale. Both approximations fail when kU is of O(1) (a). The approximation in (3.4) fails also where $|Uk| < \eta$ (b).

through (2.24) for kU small, but not too small. This approximation holds in most of the small (k, η)-domain, but fails where kU is of order η or smaller (see Fig. 5b).

Ignoring this failure for the moment, the expression in (3.1) reduces to

$$C(k, \eta) \approx \frac{1 - 4q_F s_F |kU|^{\nu_F - 1}}{\eta + 2q_F c_F |kU|^{\nu_F}}, \tag{3.4}$$

where

$$c_F \equiv |\cos(\pi \nu_F/2)|, \qquad s_F \equiv |\sin(\pi \nu_F/2)|. \tag{3.5}$$

Although the approximation (3.4) requires $|kU| \gg \eta$, it so happens that (3.1) and (3.4) are both equal to $1/\eta$ at $k = 0$. Despite this pleasant coincidence at $k = 0$, a direct comparison of (3.1) with (3.4) shows that there are important differences at small wavenumbers (see Fig. 5b). (Notice that in (2.33) the division by k^{p+1} heavily weights small k.)

Inverting the transforms in (3.4) and introducing $\tilde{t} \equiv 2q_F c_F U^{\nu_F} t$, gives

$$C(x, \tilde{t}) \approx \tilde{t}^{-1/\nu_F} \mathcal{C}_L \left(\frac{x}{\tilde{t}^{1/\nu_F}} \right) + 4q_F s_F U^{\nu_F - 1} \tilde{t}^{-1} \mathcal{C}_{FL} \left(\frac{x}{\tilde{t}^{1/\nu_F}} \right), \tag{3.6}$$

where $\mathcal{C}_L$ is a Lévy density (see [20]),

$$\mathcal{C}_L(\xi) \equiv \frac{1}{2\pi} \int_{-\infty}^{\infty} \exp(ik\xi - |k|^{\nu_F}) \, dk \tag{3.7}$$

and $\mathcal{C}_{FL}$ is a fractional derivative of a Lévy density (see [11]),

$$\mathcal{C}_{FL}(\xi) \equiv -\frac{1}{2\pi} \int_{-\infty}^{\infty} |k|^{\nu_F - 1} \exp(ik\xi - |k|^{\nu_F}) \, dk. \tag{3.8}$$

The core of the concentration $C(x, t)$ is therefore composed of a self-similar Lévy density plus a correction, given, respectively, by the first and second terms on the RHS of (3.6). The Lévy density decays as t^{-1/ν_F}, while the correction decays slightly faster as t^{-1}. Therefore at large times the concentration $C(x, t)$ relaxes to a self-similar Lévy density.

In Section 4 we make a comparison between the Lévy density, computed by numerical inversion of the transform in (3.7), and a simulation. That comparison is disappointing; the similarity form in the first term of (3.6) nicely collapses the data, but the collapsed concentration profiles depart from $\mathcal{C}_L$. This failure is because at finite times

the slowly decaying correction $t^{-1}\mathcal{C}_{NL}$ in (3.6) masks $t^{-1/\nu_F}\mathcal{C}_L$. To substantiate this claim, we show that the higher order term improves the comparison with numerical simulations in the CSR.

The tails of $C(x, t)$ at large times are given by the large-ξ expansion of $\mathcal{C}_L$,

$$C(x, \tilde{t}) \approx \frac{1}{\pi} \Gamma(\nu_F + 1) s_F \tilde{t} |x|^{-\nu_F - 1} \quad \text{for } x/\tilde{t}^{1/\nu_F} \gg 1. \tag{3.9}$$

Because of the power law in (3.9), moments computed with the Lévy approximation are infinite if $p \geq \nu_F$. Moments $p < \nu_F$ instead are finite and follow the self-similar scaling $\gamma_p = p/\nu_F$. The divergence of high moments is an artifact of the $|kU| \gg \eta$ approximation involved in passing from (3.1) to (3.4) and (3.6); the more accurate approximation in (3.1) can be used to compute all moments.

The failure of (3.6) at large x is also indicated by the fact that $C_L \sim |x|^{-1-\nu_F}$, while $C_{FL} \sim |x|^{-\nu_F}$. Thus, at fixed t, as $|x| \to \infty$, the ostensibly small correction C_{FL}, becomes larger than the leading term C_L. This non-uniformity is another symptom of the failure of (3.4) and (3.6) in the tails.

3.3. The fractional moment exponents for $1 < \nu_F < 2$ and $1 < \nu_S < 2$

The large-t growth rate of fractional moments is obtained from the integral representation of $\langle |x|^p \rangle$ in (2.33). The integral in (2.33) has an isolated branch-point at $\eta = 0$ as the rightmost singularity. Therefore the $t \to \infty$ behavior of $\langle |x|^p \rangle$ is obtained by expanding the integrand around the branch-point at $\eta = 0$ and inverting the Laplace transform. At leading order, only the local contribution from $k \ll O(1)$ contributes to the integral and we can simplify the algebra by using the small (k, η)-approximation for C in (3.1). Plugging (3.1) into (2.33), and dropping inconsequential terms of $O(\eta^{\nu_S-1})$, we obtain

$$\langle |x|^p \rangle(\eta) = \frac{2}{\pi} \Gamma(p + 1) \sin \frac{\pi p}{2} q_F U^p \eta^{-p-2+\nu_F} \int_0^\infty \frac{\Upsilon}{1 + q_F \Xi_{\nu_F} \eta^{\nu_F-1}} \frac{d\xi}{\xi^{p+1}}. \tag{3.10}$$

Above we introduced the variable $\xi \equiv kU/\eta$, and we defined the real, even function

$$\Xi_\beta(\xi) \equiv -(1 + i\xi)^\beta - (1 - i\xi)^\beta, \tag{3.11}$$

and the positive, real, even function

$$\Upsilon(\xi) \equiv \Xi_{\nu_F} - 2\Xi_{\nu_F-1} + \Xi_{\nu_F-2}. \tag{3.12}$$

The expression in (3.10) is valid if $0 < p < 2$, which suffices to capture the break in slope of γ_p at $p = \nu_F$.

To approximate the integral in (3.10), one might begin by dropping the term proportional to η^{ν_F-1} in the denominator on the RHS. Then, because the remaining η-dependence is outside the integral, the Laplace transform is easily inverted and we can conclude that $\gamma_p = p + 1 - \nu_F$. This straightforward argument is correct only if $p > \nu_F$; in this case the simplified integral converges and the main contribution comes from the neighborhood of $\xi = 0$ (small wavenumbers). But, if $p < \nu_F$, then the simplified integral diverges because at large ξ the integrand is proportional to $\xi^{\nu_F-p-1} > \xi^{-1}$.

The divergence when $p < \nu_F$ signals that the main contribution to the integral is now from the neighborhood $\xi = \infty$ (large wavenumbers). In this case, the term proportional to η^{ν_F-1} in (3.10) is no longer inconsequential: this term now secures convergence at $\xi = \infty$. To isolate the large ξ contribution, one makes the change of variable $\zeta \equiv \xi \eta^{1-1/\nu_F}$ in (3.10). After this transformation, one can again neglect all terms involving η which appear within the integral. The resulting approximation of (3.10) is

$$\langle |x|^p \rangle(\eta) = \frac{4}{\pi} \Gamma(p + 1) \sin \frac{\pi p}{2} q_F c_F U^p \eta^{-p/\nu_F-1} \int_0^\infty \frac{\zeta^{\nu_F-p-1}}{1 + 2q_F c_F \zeta^{\nu_F}} d\zeta. \tag{3.13}$$

Inverting the Laplace transform above, we conclude that $\gamma_p = p/\nu_F$. This result is correct only if $p < \nu_F$, so that the integral in (3.13) converges.

The conclusion of the previous two paragraphs is summarized by the piecewise-linear exponent γ_p in (2.37) through (2.39) for $1 < \nu_F < 2$. The two branches of γ_p are determined by different regions in wavenumber space; the $\gamma_p = p + 1 - \nu_F$ branch is produced by wavenumbers close to zero, while the $\gamma_p = p/\nu_F$ branch is the result of small, but not too small, wavenumbers. The asymptotics have been carried through only for moments $0 < p < 2$, but the numerical simulations presented in the next section show that the piecewise-linear scaling is valid also for $p > 2$.

The transition case when $p = \nu_F$ deserves some comment: precisely at this point both approximate integrals have logarithmic divergences and nothing seems to work. The cure for this is a matched asymptotic expansion, which shows that $\langle |x|^p \rangle \sim t \ln t$. More than this, we obtain a uniformly valid approximation in the neighborhood of $p = \nu_F$:

$$\langle |x|^p \rangle \approx A_p t^{p/\nu_F} + B_p t^{p+1-\nu_F} + \frac{C_p}{\nu_F - p} \left[\frac{t^{p/\nu_F}}{\Gamma(p/\nu_F + 1)} - \frac{t^{p+1-\nu_F}}{\Gamma(p + 2 - \nu_F)} \right], \tag{3.14}$$

where

$$A_p = \frac{4}{\pi} \sin \frac{\pi p}{2} \frac{\Gamma(p+1)}{\Gamma(p/\nu_F + 1)} q_F c_F U^p \left[\int_1^\infty \frac{\zeta^{\nu_F - p - 1}}{1 + 2 q_F c_F \zeta^{\nu_F}} \, d\zeta - 2 q_F c_F \int_0^1 \frac{\zeta^{2\nu_F - p - 1}}{1 + 2 q_F c_F \zeta^{\nu_F}} \, d\zeta \right], \tag{3.15}$$

$$B_p = \frac{2}{\pi} \sin \frac{\pi p}{2} \frac{\Gamma(p+1)}{\Gamma(p + 2 - \nu_F)} q_F U^p \left[\int_0^1 \frac{\Upsilon}{\xi^{p+1}} \, d\xi + \int_1^\infty \frac{\Upsilon - 2 c_F \xi^{\nu_F}}{\xi^{p+1}} \, d\xi \right], \tag{3.16}$$

and

$$C_p = \frac{4}{\pi} \sin \frac{\pi p}{2} \Gamma(p+1) q_F c_F U^p. \tag{3.17}$$

3.4. Asymptotics for the case $0 < \nu_F < 1$ and $1 < \nu_S$

With the age-dependent transition rates $\alpha_\chi(a)$ in (2.16), τ_F is infinite when $0 < \nu_F < 1$. In this case we cannot use the initial conditions in (2.18), because the equilibrium age distribution is not normalizable. Instead we take

$$[\mathcal{R}(a, x, 0), \mathcal{S}(a, x, 0), \mathcal{L}(a, x, 0)] = [\tfrac{1}{4}, \tfrac{1}{2}, \tfrac{1}{4}] \delta(a) \delta(x). \tag{3.18}$$

Thus, all particles are released at $x = 0$ with zero age, a quarter flying to the right, a quarter flying to the left and the remaining half sticking.

The initial value problem can now be solved in Laplace–Fourier space. Following the same steps sketched for the case $1 < \nu_F < 2$, we obtain the small (k, η)-approximation for the concentration C

$$C(k, \eta) \approx \frac{\Lambda_{\nu_F - 1}}{\Lambda_{\nu_F}}, \tag{3.19}$$

where $\Lambda_\beta(\eta, k)$ is defined in (3.2).

The leading order behavior in η of fractional moments is now computed by using (3.19) in (2.33):

$$\langle |x|^p \rangle(\eta) = \frac{2}{\pi} \Gamma(p+1) \sin \frac{\pi p}{2} U^p \eta^{-p-1} \int_0^\infty \frac{\Xi_{\nu_F} - \Xi_{\nu_F - 1}}{\Xi_{\nu_F}} \frac{d\xi}{\xi^{p+1}}, \tag{3.20}$$

where Ξ_β is defined in (3.11). The η-dependence in (3.20) is entirely outside the integral, and we can invert the Laplace transform to conclude that $\gamma_p = p$. The formula in (3.20) is valid only for $0 < p < 2$, but again we

use the numerical simulations in the next section to show that the scaling $\gamma_p = p$ is valid for all p. Therefore for $0 < \nu_F < 1$, diffusion is anomalous and strongly self-similar.

3.5. Comments for the case $1 < \nu_F$ and $0 < \nu_S < 1$

We briefly comment on the case $1 < \nu_F$ and $0 < \nu_S < 1$; that is, τ_S is infinite but τ_F is finite. In this case the sticking events play a major role in determining the asymptotic dispersion. Calculations similar to those presented above, using the initial condition in (3.18), give the following expression for γ_p:

$$\gamma_p = \begin{cases} \dfrac{\nu_S}{\nu_{\min}} p & \text{if } p < p_{\max}, \\ p + \nu_S - \nu_F & \text{if } p > p_{\max}, \end{cases} \tag{3.21}$$

where

$$\nu_{\min} = \min(2, \nu_F), \tag{3.22}$$

and

$$p_{\max}(\nu_F, \nu_S) = \max\left[\nu_F, 2\frac{\nu_F - \nu_S}{2 - \nu_S}\right]. \tag{3.23}$$

Notice that (3.21) predicts subdiffusion, $\gamma_2 < 1$, if $\nu_F > \nu_S + 1$. The case $\nu_F = 2\nu_S$ is amusing because the low moments follow the Gaussian scaling, $\gamma_p = \frac{1}{2}p$, even though the CSR is not Gaussian.

4. Numerical simulations of the generalized telegraph model

Numerical simulations of the generalized telegraph model have been run to illustrate the results obtained above. Numerous runs have been performed with different values of ν_F and ν_S as to present examples of both strong and weak self-similarity, and of both normal and anomalous diffusion. In most Monte Carlo simulations we release $N = 10^7$ particles at $x = 0$. If both ν_F and ν_S are larger than 1, then we use the initial age distribution in (2.18); otherwise we use (3.18). During the run, each particle may undergo a transition from flying to stationary or vice versa with the transition rate given in (2.16). The moments $\langle |x|^p \rangle$ are then computed as a function of time using (1.3). Finally, the moment exponent γ_p is obtained from a linear least-squares fit of $\log\langle |x|^p \rangle$ versus $\log t$. Although each simulation run for 10^4 time units, only the last decade of the simulation ($10^3 < t < 10^4$) is used in the fit, in order to minimize transient effects. For all runs presented, $\theta_F = \theta_S = 1$ and $U = 1$.

Fig. 6 shows the dependence of γ_p on the moment p for a run with $\nu_F = 1.3$ and $\nu_S = 1.6$. The scaling obtained by the Monte Carlo simulations (dots) agrees with the piecewise-linear prediction given in (2.37) (continuous lines); that is the system exhibits anomalous diffusion ($\gamma_2 > 1$) and weak self-similarity. Fig. 6b is an expanded view of Fig. 6a for $1 < p < 2$ to show in detail the exchange of dominance of the moment exponents. The γ_p estimated from the simulations overestimates the piecewise-linear prediction in the neighborhood of $p = \nu_F$. This overestimate is a finite time effect as can be verified by computing γ_p from a linear fit of the expression in (3.14) for times between $10^3 < t < 10^4$.

The concentrations at various times are plotted in Fig. 7, using the similarity scaling in (1.2) with $\nu = \nu_F$. The δ-peaks at $x = \pm Ut$ correspond to particles that have never transitioned from their original state. These peaks decay algebraically in time as $t^{1-\nu_F}$ in agreement with the result in (2.25) and (2.26). The Lévy density in (3.7) is superimposed as a dashed line on the Monte Carlo concentrations. The agreement between the Lévy density and
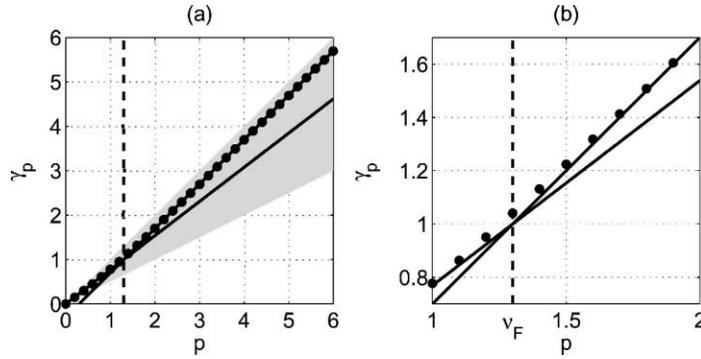
Fig. 6. (a) Moment exponents γ_p with $0 < p < 6$. The moments are computed from Monte Carlo simulations of the generalized telegraph model with $N = 10^7$ particles, $\nu_F = 1.3$, $\nu_S = 1.6$, $\theta_F = \theta_S = 1$ and $U = 1$. The dots are the results of numerical simulations, while the continuous lines are the two branches of the theoretical piecewise-linear scaling in (2.37) through (2.39) with $\nu_F = 1.3$. The vertical dashed line is at $p = \nu_F$, where the two branches of the scaling intersect. The shaded wedge is the region between the diffusive law $\gamma_p = \frac{1}{2}p$ and the ballistic law $\gamma_p = p$. (b) An enlargement of (a) for $1 \leq p \leq 2$.

the simulations is not satisfactory. The Monte Carlo concentrations depart from the Lévy distribution in the tails *and* at $x = 0$. As mentioned in Section 3.2 the disagreement at $x = 0$ is due to finite time effects. The disagreement in the tails is because the Lévy approximation is not valid at large x.

Fig. 8 shows that closer agreement in the core can be obtained by just retaining the extra term in (3.6). The improved approximation is closer to the Monte Carlo simulation in the CSR and particularly at $x = 0$, but, as expected, there are still strong discrepancies in the tails.

It has been shown in (2.30) and (2.31) that the contribution of the δ-peaks at $x = \pm Ut$ to the moment $\langle |x|^p \rangle$ is proportional to $t^{p+1-\nu_F}$ for large times.

However the high-moment branch of γ_p shown in Fig. 6 is not due only to these ballistic particles. This can be tested against simulations by recomputing all moments using only particles that underwent at least one transition between sticking and flying; that is,
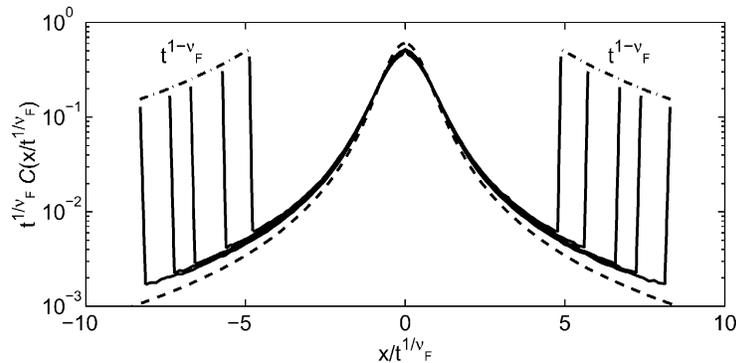

Fig. 7. Concentration $C(x, t)$ at selected times in the last decade of the same Monte Carlo simulation used for Fig. 6. The amplitude of the concentration and the x-axis are rescaled with the factor t^{1/ν_F} to show the self-similar nature of the CSR. The dashed line is the self-similar Lévy density to which the Monte Carlo concentrations should converge at large times. The dash–dotted lines show the algebraic decay of the δ-peaks at $x = \pm Ut$. A small δ-peak is present at $x = 0$ and is due to the sticking particles that have never transitioned.
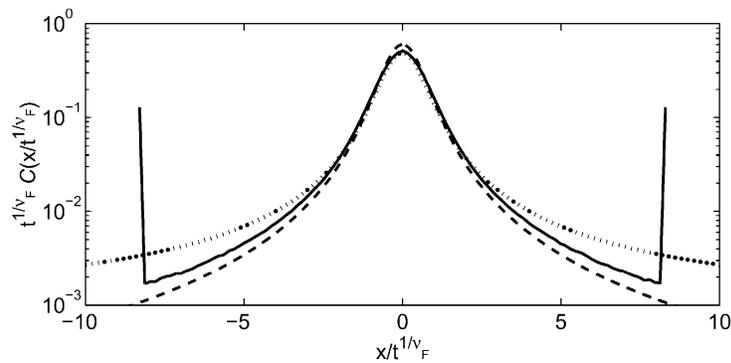
Fig. 8. Concentration $C(x, t)$ as in Fig. 7, but only at $t = 10^4$. The Monte Carlo concentration (continuous line) is compared with the Lévy density given by the first term on the RHS of (3.6) (dashed line) and the full expression in (3.6) (dotted line).

$$\langle |x|^p \rangle' \equiv \frac{1}{N'} \sum_{n=1}^{N'} |x_n(t)|^p, \tag{4.1}$$

where $N'(t)$ is the number of particles that has undergone at least one transition at time t. This is equivalent to computing moments from the concentrations after excising the δ-peaks. Linear fitting the γ_p from moments computed in this way gives the same results as in Fig. 6a. Therefore either the δ-peaks or the tails are sufficient to produce the $p + 1 - \nu_F$ branch of γ_p.

Fig. 9 is the result of a run with $\nu_F = 2.2$ and $\nu_S = 1.6$. Because $\nu_F > 2$, diffusion is normal, the central limit theorem applies, and there is a CSR within which the concentration profile is Gaussian and $\gamma_p = \frac{1}{2} p$. But the tails of the concentration are not self-similar and moments $p > 2(\nu_F - 1)$ follow the different scaling $\gamma_p = p + 1 - \nu_F$; that is self-similarity is weak, in agreement with (2.37). In the simulations the convergence towards the upper branch of the piecewise-linear scaling is slow. The implication is that for p close to $2(\nu_F - 1)$, the two leading order terms in the growth rate of moments are

$$\langle |x|^p \rangle \approx A_p t^{p/2} + B_p t^{p+1-\nu_F} \quad \text{for} \ p \approx 2(\nu_F - 1), \tag{4.2}$$
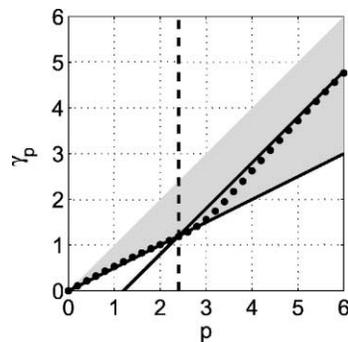

Fig. 9. Moment exponents γ_p with $0 < p < 6$. The moments are computed from Monte Carlo simulations of the generalized telegraph model with $\nu_F = 2.2$ and $\nu_S = 1.6$. The continuous lines are the two branches of the theoretical piecewise-linear scaling in (2.37) through (2.39) with $\nu_F = 2.2$. All other parameters and curves are the same as in Fig. 6. The two branches of the theoretical scaling meet at $p = 2(\nu_F - 1)$, shown as a vertical dashed line.
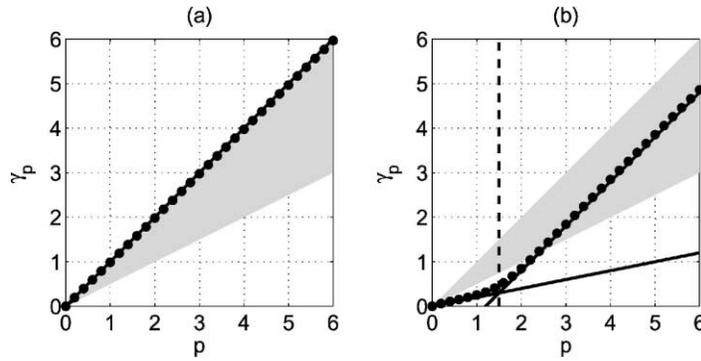
Fig. 10. Moment exponents γ_p with $0 < p < 6$. The moments are computed from Monte Carlo simulations of the generalized telegraph model. (a) Run with $\nu_F = 0.7$ and $\nu_S = 1.6$. The continuous line is the theoretical ballistic scaling. (b) Run with $\nu_F = 1.5$ and $\nu_S = 0.3$. The two continuous lines correspond to the theoretical scaling in (3.21) through (3.23). The vertical dashed line is at $p = \nu_F$. All other parameters and curves are the same as in Fig. 6.

and both A_p and B_p are positive, but $A_p \gg B_p$. In this case, as in Fig. 9, at finite times a linear least-squares fit underestimates γ_p for $p > 2(\nu_F - 1)$; the scaling of high moments is recovered only for p sufficiently large.

The results in Fig. 10a are obtained from a simulation with $\nu_F = 0.7$ and $\nu_S = 1.6$ and the initial conditions in (3.18). For $\nu_F < 1$, diffusion is ballistic, that is $\gamma_p = p$ for all p. This is an example of anomalous diffusion and strong self-similarity.

Finally, Fig. 10b shows the results of a run with $\nu_F = 1.5 > 1$ and $\nu_S = 0.3 < 1$. As predicted in Section 3.5 $\gamma_p = p\nu_S/\nu_F$ for $p < \nu_F$ and $\gamma_p = p + \nu_S - \nu_F$ for $p > \nu_F$. In this run the system is subdiffusive and weakly self-similar.

We close this section with some remarks on the sensitivity of the results to the number of particles in the simulations. Of course an accurate estimate of γ_p depends critically on the number of particles N; above we have used $N = 10^7$, which is overkill. Typically the core of the concentration is easy to resolve even with a few particles, e.g. $N = 10^3$. But resolving the tails may require more particles. This problem is most severe when the transition rates are high, e.g., $\nu_\chi > 2$. In these cases it is necessary to use $N = 10^7$ to obtain satisfactory results. On the other hand, when the transition rates are low, e.g., $\nu_\chi < 2$, fewer particles suffice. This point is important considering that
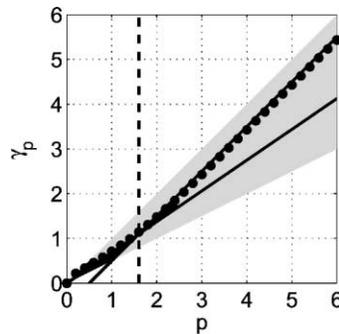

Fig. 11. Moment exponents γ_p with $0 < p < 6$. The moments are computed from Monte Carlo simulations of the generalized telegraph model with $N = 10^3$ particles, $\nu_F = 1.6$, $\nu_S = 1.1$, $\theta_F = \theta_S = 1$ and $U = 1$. The dots are the results of a linear least-squares fit of $\log\langle |x|^p \rangle$ versus $\log t$ for $10^2 < t < 10^3$. The continuous lines are the two branches of the theoretical piecewise-linear scaling. The vertical dashed line is at $p = \nu_F$.

the experiments in [7] use typically $N = 10^3$ particles. In Fig. 11 we show the results from the simulations with parameter values suggested by Solomon et al. [7]. Because $\nu_F = 1.6$ and $\nu_S = 1.1$, the transition rates are low and, even with $N = 10^3$ particles, the piecewise-linear relation is plain for $10^2 < t < 10^3$.

5. A deterministic area-preserving map

In the previous sections we introduced a stochastic model and showed using a combination of analysis and simulations that the moment exponent, γ_p, is a piecewise-linear function of p, as in Fig. 2. In this section we show that the same is characteristic of a deterministic area-preserving map. This map, known as the "kicked Harper map" [21], exhibits a flight–stick phenomenology which resembles both experiments and the generalized telegraph model.

5.1. The kicked Harper map

We introduce the kicked Harper map as a model of a two-dimensional incompressible flow consisting of persistent vortices separated by jets. The incompressibility condition means that we can specify the flow in terms of a streamfunction $\psi(x, y, t)$. The motion of a particle advected by the fluid is obtained by integrating

$$\dot{x} = -\frac{\partial \psi}{\partial y}, \qquad \dot{y} = \frac{\partial \psi}{\partial x}. \tag{5.1}$$

Eq. (5.1) are just Hamilton's equations for a one degree of freedom system, if we identify the streamfunction $\psi(x, y, t)$ with the Hamiltonian and x and y with the conjugate coordinates. The path of a particle in a two-dimensional flow is, therefore, the phase-space trajectory of the corresponding Hamiltonian system. If ψ is time independent, the equations of motion are fully integrable and trajectories follow streamlines. Let us consider the streamfunction

$$\psi(x, y) = \tfrac{1}{2}(\cos y - \mu \cos x), \quad 0 \le \mu \le 1. \tag{5.2}$$

In this flow there are chains of vortices sandwiched between jets (Fig. 12). The parameter μ controls the relative thickness of jets and vortices. For $\mu = 0$ the flow is composed of alternating unidirectional jets parallel to the x-axis. Vortices appear for $0 < \mu < 1$ and fill all the space as μ approaches 1. Without loss of generality we take $0 \le \mu \le 1$.

Particles dropped in this steady flow are either permanently trapped in vortices or permanently flying in jets. More complicated trajectories can be obtained by introducing some time dependence. Let us assume that the x and y-velocities determined by (5.2) alternate on and off sequentially. Thus a particle is advected only in x for a time interval τ, and then only in y for the following time interval τ:

$$\dot{x} = \sin y, \qquad \dot{y} = 0 \quad \text{for } 2n\tau \le t \le (2n+1)\tau, \qquad \dot{x} = 0,$$
$$\dot{y} = \mu \sin x \quad \text{for } (2n+1)\tau \le t \le 2(n+1)\tau \tag{5.3}$$

for $n = 0, 1, 2, 3 \ldots$. In each interval of duration τ the equations of motion can be easily integrated. Thus the ordinary differential equations in (5.3) are reduced to an area-preserving map,

$$x_{n+1} = x_n + \tau \sin y_n, \qquad y_{n+1} = y_n + \mu \tau \sin x_{n+1}, \tag{5.4}$$

where x_n and y_n are the positions of the particle at times $t = 2n\tau$. Fig. 12 shows a few steps of the discrete map overlaid over the continuous streamfunction (5.2). This map, known in the literature as the kicked Harper map [21–23], is an example of the "non-twist" maps described by del-Castillo-Negrete, Greene and Morrison [1,24,25].
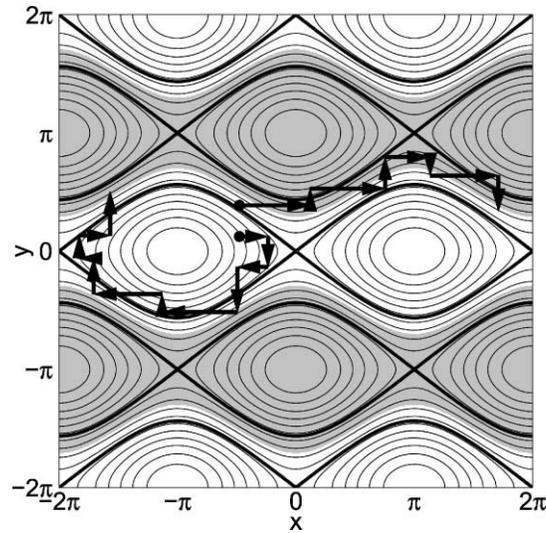
Fig. 12. A contour plot of the streamfunction in (5.2) for $\mu = 0.6$. Gray areas correspond to negative value of the streamfunction and white areas to positive values. The thick lines are the separatrices that divide jets and vortices. The arrows correspond to a few iterations of the kicked Harper map in (5.4) with $\tau = 2$ for a particle released in a vortex and a particle released in a jet.

As $\tau \to 0$, with fixed μ, the particle paths look like the streamlines of the integrable system in (5.2). In fact, the particle positions at times $2n\tau$ and $(2n + 1)\tau$ can be viewed as the odd and even steps of an operator splitting scheme, with timestep 2τ, aimed at integrating numerically the flow given by (5.2) [26]. A few integrable trajectories obtained with small τ are shown in the upper panels of Figs. 13 and 14. The map is iterated $n = 500$ times for five
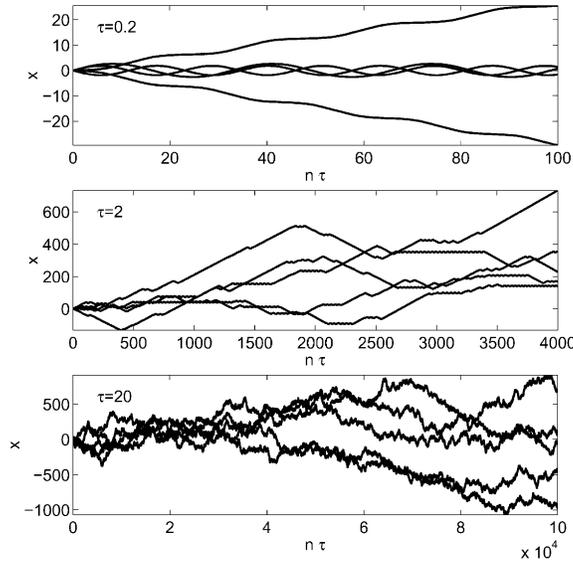

Fig. 13. The x-component of five sample trajectories for the kicked Harper map with $\mu = 0.6$ for three different values of τ. Particles are released in a square of size 2π centered on the origin. The x-positions are plotted as a function of time $t = n\tau$. The middle panel shows the flight–stick transitions which occur if τ is of order unity.
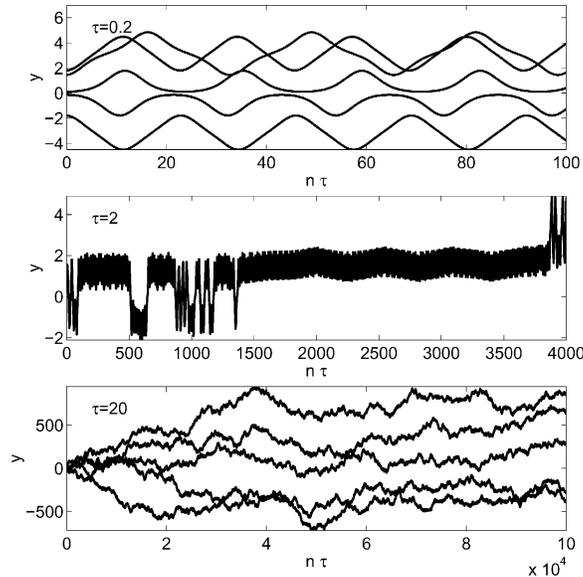
Fig. 14. The *y*-component of the trajectories in Fig. 13. To avoid clutter, only one trajectory is shown for $\tau = 2$ (middle panel).

different initial conditions with $\mu = 0.6$ and $\tau = 0.2$. Particles released in a vortex are permanently trapped, while particles released in a jet permanently fly along the *x*-axis. At this value of τ there is a only small stochastic layer surrounding the separatrix.

Increasing τ expands the stochastic layer, and particles in this region alternate chaotically between being trapped in a vortex and flying in a jet (middle panels of Figs. 13 and 14). Notice that the flights in the middle panel of Fig. 13 have a well-defined average velocity; this is rationalized because particles in the stochastic layer are averaging the underlying $\sin y$ profile in (5.4). It is in this parameter range, with τ of order unity, that we find the flight–stick transitions, anomalous diffusion and weak self-similarity which is the focus of the next section.

When τ is large there are no barriers to transport in *y*. The entire domain is densely covered by a single orbit. Trajectories become extremely erratic and look like random walks. There is no sign of vortices and jets in the particle trajectories (bottom panels of Figs. 13 and 14). If $\tau \gg 2\pi$ then the diffusivities in both the *x* and *y*-directions can be estimated with a random phase approximation.

5.2. Dispersion of an ensemble

We iterated the map in (5.4) 10^4 times using many different values of τ and μ. As an initial condition 10^7 particles are randomly placed in the $2\pi \times 2\pi$ square and the moments in (1.3) are calculated with $0 < p < 6$. The moment exponents, γ_p, are then estimated by a linear least-squares fit between $\log \langle |x|^p \rangle$ and $\log n$ using only iterations in the interval $500 < n < 3{,}000$. This interval is chosen to ensure that the few particles on integrable trajectories do not bias the results, as discussed below.

The exploration of the μ–τ parameter space suggested that diffusion is normal and strongly self-similar for large values of the product $\mu\tau$, while it is ballistic and strongly self-similar for small values of $\mu\tau$. Between these two regimes, with $\mu\tau = \mathrm{O}(1)$, there is diffusion which is weakly self-similar and either normal or anomalous. We discuss this case in some detail below.

The case $\mu = 1$ is special, because as $\tau \to 0$ there are no jets and consequently no possibility of ballistic transport. Nevertheless, with $\mu = 1$, there are a few values of τ for which diffusion is anomalous because of accelerator modes [21], rather than because of ballistic transport in jets. Our interest is mainly in flows dominated by jets and vortices, so we will not discuss the jetless case $\mu = 1$ in detail. Nonetheless, we cannot resist speculating that the "puzzling fact" observed by Leboeuf, (namely, not all accelerator modes produce anomalous diffusion) is rationalized if the exponent ν_F is greater than 2. To test this speculation one could look for normal, but weakly self-similar, diffusion due to these accelerator modes.

For the discussion in this section we focus on two sets of μ–τ values:

1. In (5.4), $\tau = 2$ and $\mu = 0.6$. The diffusion in x is anomalous, with $\gamma_2 \approx 1.53$, while the ensemble is localized in the y-direction.
2. In (5.4), $\tau = 4.2$ and $\mu = 0.35$. The diffusion in x is normal, that is $\gamma_2 = 1$, while the ensemble is localized in the y-direction.

In both cases above the piecewise-linear structure of γ_p, is clear (see Fig. 15). The parameter ν_F is then determined by a nonlinear least-squares fit of γ_p from the simulations to the piecewise-linear function in (2.37).

In the first case (Fig. 15a) we find from the bilinear fit that $\nu_F = 1.55$. Using this number, we can then demonstrate the existence of a CSR by taking concentration profiles at different times and using the similarity scaling in (1.2). Fig. 16 shows that there is a central region in which the various concentration profiles collapse onto a single function. The non-scaling tails, and the algebraically decaying ballistic peaks — with the exponent $1 - \nu_F$ suggested by the generalized telegraph model — are also evident. Thus the generalized telegraph model captures the main features of this deterministic example.

We close this section with some comments on the most annoying technical problem we encountered in the estimation of γ_p, in Fig. 15. Hidden in the ensemble of 10^7 particles there are a few particles which are on integrable trajectories. These "integrable particles" are either permanently flying, or permanently stuck in a single vortex. At very long times the permanently flying particles will produce $\gamma_p = p$ for all p. Thus to determine γ_p it is necessary to avoid very long times. Instead we use a restricted time interval over which the effects of the integrable particles are diluted by the majority of tail particles, which are in the stochastic layer. In practice we found that $500 < n < 3,000$ is a good compromise.
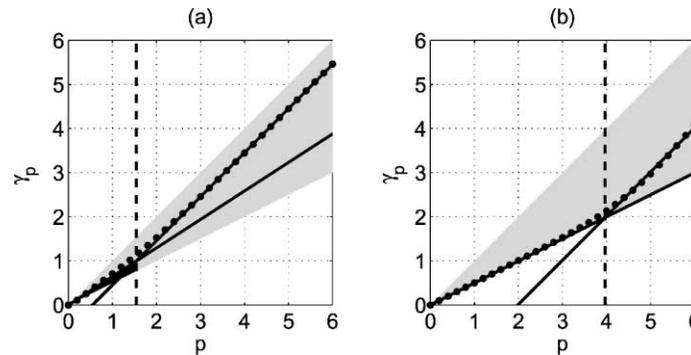

Fig. 15. Moment exponents γ_p with $0 < p < 6$. The moments are computed by iterating the kicked Harper map for $n = 10^4$ steps with 10^7 particles. (a) Results for $\tau = 2$ and $\mu = 0.6$. (b) Results for $\tau = 4.2$ and $\mu = 0.35$. The dots are the results of numerical simulations, while the continuous lines are the two branches of the piecewise-linear function in (2.37). The parameter ν_F in those equations is obtained by fitting the piecewise-linear prediction to the numerical results: $\nu_F = 1.55$ in (a) and $\nu_F = 2.98$ in (b). The vertical dashed lines indicate where the two branches of the scaling intersect, that is at $p = \nu_F$ in (a) and $p = 2(\nu_F - 1)$ in (b). The shaded wedge is the region between the diffusive law $\gamma_p = \frac{1}{2} p$ and the ballistic law $\gamma_p = p$.
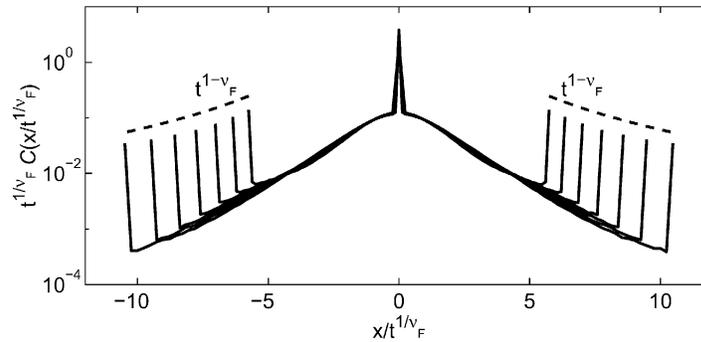
Fig. 16. Rescaled concentrations of particles for the simulation of Fig. 15a. Seven different concentration profiles are shown for iterations of the map between $500 < n < 3,000$.

6. Conclusions

In this article we have introduced a formula (2.33) which enables one to extract the pth moment of the concentration from the Laplace–Fourier representation of the propagator. Using (2.33) we have shown that flight–stick stochastic systems with an asymptotic transition rate $\alpha_\chi \sim \nu_\chi/a$ (the age, a, is the time which has elapsed since the particle transitioned into its present state) have moment exponents, γ_p, with a characteristic piecewise-linear form. The small-p branch, which passes through the origin of the (p, γ_p) plane, indicates the existence of a CSR containing most of the particles. The large-p branch is determined by relatively few tail particles which have experienced large displacements. Depending on the details of the dispersive process, the much studied exponent γ_2 might lie on either of the two branches.

If γ_2 is on the large-p branch, then one should be sensitively aware that the dispersion of the majority of particles will not follow the scaling suggested by measurements of $\langle x^2 \rangle$. A cautionary illustration of this issue is provided by taking $\nu_F = 1.5$ and $\nu_S = 0.5$ in the generalized telegraph model. Then, from (3.21) through (3.23), one finds that $\gamma_2 = 1$. According to the standard definition, this is normal diffusion. However the CSR is non-Gaussian and indeed the similarity variable is $x/t^{1/3}$, *not* $x/t^{1/2}$ (see Fig. 17). This is an example of what might be called "accidental normal diffusion", as opposed to the normal diffusion resulting from the central limit theorem.
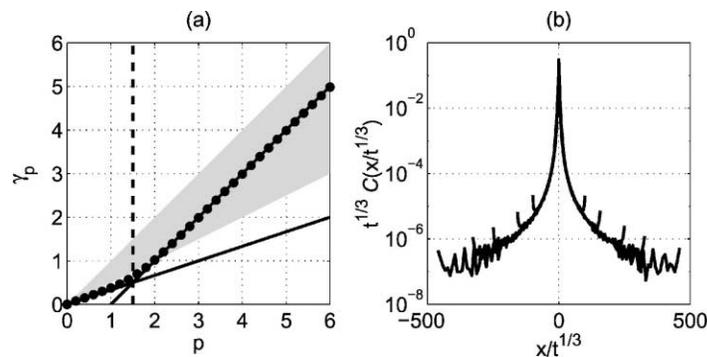

Fig. 17. Moment exponents γ_p, with $0 < p < 6$ (a) and rescaled concentration at selected times in the last decade, $10^3 < t < 10^4$, (b) of a Monte Carlo simulation of the generalized telegraph model with $\nu_F = 1.5$ and $\nu_S = 0.5$. All other parameters and curves are the same as in Figs. 6 and 7. The concentration is clearly non-Gaussian, but $\gamma_2 = 1$. Therefore this is an example of weakly self-similar normal diffusion without a Gaussian core.

Amusing examples like the one in the previous paragraph are easy to construct with the generalized telegraph model. It is more impressive that the piecewise-linear γ_p relation is not just an accident of the analysis which is possible for the generalized telegraph equation; at certain points in the (μ, τ) parameter plane, the kicked Harper map, (5.4), also has a piecewise-linear γ_p. The most general characterization of such systems is that the transition rate between the flying and sticking states has the large-a form $\alpha_\chi \sim \nu_\chi / a$.

Why should we expect that $\alpha_\chi \sim \nu_\chi / a$ for a deterministic system? The glib answer is that if one wants power laws such as (1.4) then $\alpha_\chi \sim \nu_\chi / a$ does the trick. A more satisfactory answer is provided by dimensional analysis, and a little assumption: the transition rate α_χ has the dimensions of inverse time. If a particle has been in the flying for a very long time, a, then it is plausible that a itself is the only relevant time-scale which can determine the transition rate. Of course, determining the behavior of the survival probability, $\Psi_\chi(a)$, for a given chaotic system is non-trivial (for example, see [27–29]). But there the issue is to express the non-dimensional constant ν_χ as a function of the system parameters, rather than to simply rationalize $\alpha_\chi \sim a^{-1}$ as we have done above.

At any rate, the assumption that $\alpha_F \sim \nu_F / a$ can be tested stringently by showing that γ_p has the piecewise-linear structure predicted by the generalized telegraph model. The test is stringent because one is using only on a *single* parameter, ν_F, to fit a nonlinear function such as (2.37)–(2.39).

We have emphasized that γ_p provides more information than γ_2. But γ_p also contains less information than the full concentration. So what are the advantages of using γ_p? It has been our consistent experience that clean functional forms for γ_p emerge at relatively early times and with a modest number of particles. By contrast, convincingly demonstrating self-similar collapse of the concentration profiles is much more difficult. It is even more difficult to show that concentration profiles match analytic forms, such as the Lévy density (e.g. Fig. 7). Slow convergence towards the ultimate Lévy density, coupled with the failure of this approximation in the tails, means that fractional kinetic equations have limited utility for the dispersive processes discussed in this paper.

Another advantage of γ_p is that it is easy to measure $\langle |x|^p \rangle$ when p is small. The slope of γ_p, at $p = 0$ is perhaps one of the best ways of inferring the scaling exponents of the CSR. Moreover the break in slope is easily identified and the location of γ_2 relative to this break conveys more information than the simple dichotomy between normal and anomalous diffusion.

We close with some remarks on the importance of our results for transport in chaotic Hamiltonian systems. It is a widely received opinion that in Hamiltonian transport the self-similar dispersion of the core of the concentration results from the scaling properties of the islands-round-islands structure of the phase space. Thus, using renormalization, the exponent ν in (1.2) can be related to the scaling constants which characterize island geometry. This procedure also results in a 'Fractional-Fokker–Planck–Kolmogorov (FFPK) equation' which is an integro-differential equation with algebraically decaying kernels. The long-time behavior of the propagator core is the similarity solution (1.2) of the FFPK equation (for a good review, see [28]). In our opinion an important limitation of this program is that the FFPK equation contains no information about the tails of the propagator. This omission would be unimportant if the tails were non-universal. But for some systems, such as the standard map [16] and the kicked Harper map, the relations (2.37)–(2.39) imply that the entire structure of the propagator, both the CSR and the tails, can be characterized by the single parameter ν_F. In this sense there is important universal structure in the tails. An asymptotic description which encompasses both regimes seems only to be possible in Fourier space. In other words, while transforms such as (3.1) successfully capture both the core and the tails, the physical space version of these results is much more complicated than the FFPK equation.

Acknowledgements

Appendix A. Laplace–Fourier solution of the generalized telegraph model

In Laplace–Fourier space the system in (2.1) and (2.2) becomes

$$\eta \mathcal{R} + \mathcal{R}_a + ikU\mathcal{R} + \alpha_F \mathcal{R} = r\Psi_F(a), \qquad \eta \mathcal{L} + \mathcal{L}_a - ikU\mathcal{L} + \alpha_F \mathcal{L} = r\Psi_F(a), \tag{A.1}$$

$$\eta \mathcal{S} + \mathcal{S}_a + \alpha_S \mathcal{S} = 2r\Psi_S(a), \tag{A.1}$$

where the terms on the right-hand side follow from the initial conditions in (2.18). The system in (A.1) can be solved,

$$\mathcal{R} = \mathcal{R}(0, k, \eta)\Psi_F(a)\, e^{-\eta_+ a} + r\Psi_F(a)\frac{1 - e^{-\eta_+ a}}{\eta_+}, \tag{A.2}$$

$$\mathcal{L} = \mathcal{L}(0, k, \eta)\Psi_F(a)\, e^{-\eta_- a} + r\Psi_F(a)\frac{1 - e^{-\eta_- a}}{\eta_-}, \tag{A.3}$$

$$\mathcal{S} = \mathcal{S}(0, k, \eta)\Psi_S(a)\, e^{-\eta a} + 2r\Psi_S(a)\frac{1 - e^{-\eta a}}{\eta}, \tag{A.4}$$

where $\eta_+ = \eta + ikU$ and $\eta_- = \eta - ikU$. The functions $\mathcal{R}(0, k, \eta)$, $\mathcal{L}(0, k, \eta)$ and $\mathcal{S}(0, k, \eta)$ are determined by imposing the karmic rules in (2.3) and (2.4),

$$\mathcal{R}(0, k, \eta) = \mathcal{L}(0, k, \eta) = \frac{r}{\eta}\frac{\Sigma + \Psi_S - \eta\Psi_S\Sigma}{\Sigma + \Delta + \Psi_S - \eta\Psi_S(\Sigma + \Delta)}, \tag{A.5}$$

$$\mathcal{S}(0, k, \eta) = \frac{2r}{\eta}\frac{\Sigma + \Psi_S - \eta\Psi_S(\Sigma + \Delta)}{\Sigma + \Delta + \Psi_S - \eta\Psi_S(\Sigma + \Delta)}. \tag{A.6}$$

In (A.5) and (A.6) all variables are in transform space, e.g. $\Psi_S = \Psi_S(\eta)$. The definitions of Σ and Δ are given in (2.21).

Finally by integrating over all ages the sum of the flying and sticking particle concentrations, $\mathcal{R} + \mathcal{L} + \mathcal{S}$, we obtain the expression in (2.22) for the concentration $C(k, \eta)$.

References

[1] D. del-Castillo-Negrete, P.J. Morrison, Chaotic transport by Rossby waves in shear flow, Phys. Fluids A 5 (1993) 948–965.
[2] W.R. Young, Arrested shear dispersion and other models of anomalous diffusion, J. Fluid. Mech. 193 (1988) 129–149.
[3] D. del-Castillo-Negrete, Asymmetric transport and non-Gaussian statistics of passive scalars in vortices in shear, Phys. Fluids 10 (1998) 576–594.
[4] J. Klafter, M.F. Schlesinger, G. Zumofen, Beyond Brownian motion, Phys. Today 49 (1996) 33–39.
[5] S. Kovalyov, Phase space structure and anomalous diffusion in a rotational fluid experiment, Chaos 10 (2000) 153–165.
[6] O. Cardoso, B. Gluckmann, O. Parcollet, P. Tabeling, Dispersion in a quasi-two-dimensional turbulent flow: an experimental study, Phys. Fluids A 8 (1996) 209–214.
[7] T.H. Solomon, E.R. Weeks, H.L. Swinney, Chaotic advection in a two-dimensional flow: Lévy flights and anomalous diffusion, Physica D 76 (1994) 70–84.
[8] E.R. Weeks, J.S. Urbach, H.L. Swinney, Anomalous diffusion in asymmetric random walks with a quasi-geostrophic flow example, Physica D 97 (1996) 291–310.
[9] M.F. Schlesinger, G.M. Zaslavsky, U. Frisch, Lévy Flights and Related Topics in Physics, Springer, Berlin, 1995, 347 pp.
[10] G. Zumofen, J. Klafter, Scale-invariant motion in intermittent chaotic systems, Phys. Rev. B 47 (1993) 851–863.
[11] A. Saichev, G.M. Zaslavsky, Fractional kinetic equations: solutions and applications, Chaos 7 (1997) 753–764.
[12] U. Frisch, Turbulence: The Legacy of A.N. Kolmogorov, Cambridge University Press, Cambridge, 1995, 296 pp.
[13] I.S. Aranson, M.I. Rabinovich, L.Sh. Tsimring, Anomalous diffusion of particles in regular fields, Phys. Lett. A. 151 (1990) 523–528.
[14] A.S. Pikovsky, Statistical properties of dynamically generated anomalous diffusion, Phys. Rev. A 43 (1991) 3146–3148.

[15] B.A. Carreras, V.E. Lynch, D.E. Newman, G.M. Zaslavsky, Anomalous diffusion in a running sandpile model, Phys. Rev. E 60 (1999) 4770–4778.

[16] P. Castiglione, A. Mazzino, P. Muratore-Ginanneschi, A. Vulpiani, On strong anomalous diffusion, Physica D 134 (1999) 75–93.

[17] K.H. Andersen, P. Castiglione, A. Mazzino, A. Vulpiani, Simple stochastic models showing strong anomalous diffusion, Eur. Phys. J. B 18 (2000) 447–452.

[18] P.M. Morse, H. Feshbach, Methods of Theoretical Physics, Part I, McGraw-Hill, New York, 1953, 997 pp.

[19] J. Klafter, G. Zumofen, Dynamically generated enhanced diffusion: the stationary state case, Physica A 196 (1993) 102–115.

[20] H.D. Hughes, Random Walks and Random Environments, Clarendon Press, Oxford, 1995, 631 pp.

[21] P. Leboeuf, Normal and anomalous diffusion in a deterministic area-preserving map, Physica D 116 (1998) 8–20.

[22] R.A. Pasmanter, From chaotic advection to chaotic Schroedinger-type equations, Phys. Rev. A 42 (1990) 3622–3625.

[23] T. Geisel, R. Ketzmerick, G. Petschel, Metamorphosis of a Cantor spectrum due to classical chaos, Phys. Rev. Lett. 67 (1991) 3635–3638.

[24] D. del-Castillo-Negrete, J.M. Greene, P.J. Morrison, Area preserving nontwist maps: periodic orbits and transition to chaos, Physica D 91 (1996) 1–23.

[25] P.J. Morrison, Magnetic field lines, Hamiltonian dynamics, and nontwist maps, Phys. Plasmas 7 (2000) 2279–2289.

[26] H. Aref, Stirring by chaotic advection, J. Fluid. Mech. 143 (1984) 1–21.

[27] C.F.F. Karney, Long-time correlations in the stochastic regime, Physica D 8 (1983) 360–380.

[28] G.M. Zaslavsky, M. Edelman, B.A. Niyazov, Self-similar, renormalization, and phase space nonuniformity of Hamiltonian chaotic dynamics, Chaos 7 (1997) 159–181 .

[29] Y.-C. Lai, M. Ding, C. Grebogi, R. Blümel, Algebraic decay and fluctuations of the decay exponent in Hamiltonian systems, Phys. Rev. A 46 (1992) 4661–4669.